

3D-WAG: Hierarchical Wavelet-Guided Autoregressive Generation for High-Fidelity 3D Shapes

Tejaswini Medi¹

tejaswini.medi@uni-mannheim.de

Arianna Rampini²

arianna.rampini@autodesk.com

Pradyumna Reddy²

printhala.pradyumna.reddy@autodesk.com

Pradeep Kumar Jayaraman²

pradeep.kumar.jayaraman@autodesk.com

Margret Keuper^{1,3}

keuper@uni-mannheim.de

¹ Chair for Machine Learning

University of Mannheim

Germany

² Autodesk AI Lab

³ MPI for Informatics

Saarland Informatics Campus

Germany

Abstract

Autoregressive (AR) models excel in language and image generation, but their role in 3D generation faces high computational cost and resolution challenges. Existing 3D AR methods, using voxel grids or implicit representations, produce long, redundant token sequences, limiting high-fidelity 3D shape generation and incurring high inference cost. To address these issues, we introduce 3D-WAG, a novel autoregressive framework employing compact wavelet-based hierarchical representations for efficient and expressive 3D shape generation. By representing the shapes in the wavelet domain, 3D-WAG captures coarse to fine geometric details as multi-scale discrete token maps, using a 3D vector-quantized variational autoencoder (VQVAE), enabling efficient AR modeling and detailed shape understanding. Unlike conventional next-token prediction, 3D-WAG formulates 3D shape generation as a next-scale token map prediction problem, achieving a faster inference time of 1.15 seconds per sample on a single NVIDIA H100 GPU, which is 15 times faster than the state-of-the-art diffusion-based 3D generation model UDiFF. Furthermore, 3D-WAG supports unconditional, class-conditional, and text-conditional shape generation. Experimental results on standard 3D benchmarks, including ShapeNet and DeepFashion3D, show that 3D-WAG outperforms state-of-the-art methods on metrics such as Minimum Matching Distance (MMD) and Coverage (COV), generating high-quality 3D shapes that accurately represent real-world data distributions.

1 Introduction

The transformative power of autoregressive (AR) models, exemplified by the GPT series [0, 1, 58, 60, 61] and subsequent advancements [2, 3, 15, 22, 55, 73, 74, 76, 77], has revolutionized natural language processing. AR models have also shown significant promise in image generation, with pioneering works such as VQGAN [91] and DALL-E [63], and



Figure 1: 3D-WAG overview. We propose an autoregressive approach to 3D shape generation, based on the “next-scale” prediction paradigm. *Left*: Our hierarchical, multi-scale wavelet encoding enables the efficient generation of highly detailed surfaces, outperforming prior models (e.g., UDiFF [102], in the red box) for comparable latent code dimensionality, and showcasing generalization in conditional 3D generation tasks, like text-to-3D. *Right*: Unconditional generation of diverse, high-fidelity shapes, supporting varied implicit spatial representations using our approach.

more recent developments [57, 65, 90], showcasing their potential. Notably, recent studies [42, 75, 93] have demonstrated that AR models, through advancements in image tokenization and training data augmentation, can surpass diffusion models in image generation tasks. This growing body of research underscores the versatility and efficacy of autoregressive modeling, hinting at its vast potential for exploration in diverse domains.

However, the full potential of AR models in 3D shape generation remains largely untapped. While several works have explored AR models for 3D synthesis [11, 64, 66, 67, 72, 88], the breakthroughs that have enabled AR models to outperform diffusion models in other domains have yet to effectively translate to 3D. Existing 3D AR methods, which sequentially predict “next tokens” to model geometric structures, primarily operate on voxels, triangles, or point coordinates. These approaches face two fundamental challenges: firstly, generating high-resolution 3D shapes requires predicting prohibitively long sequences of fine-grained tokens, leading to immense computational costs; secondly, a focus on token-by-token prediction often compromises global geometric structure. This leads to limited detail with slow predictions, resulting in incoherent shapes. Despite high inference costs [80, 95], diffusion-based models have thus become the dominant choice for 3D shape generation [12, 25, 26, 68, 66, 69].

To address the limitations of autoregressive (AR) models in 3D shape generation, we propose 3D Hierarchical Wavelet-Guided Autoregressive Generation (3D-WAG), a novel framework leveraging compact hierarchical wavelet representations, which are recently also being used in diffusion-based generation models [53, 102]. Wavelet representation allows for efficient capture of multi-scale shape information from coarse to fine, utilizing low and high frequency details of wavelets, enabling direct modeling of shapes and avoiding 2D-to-3D translation artifacts in generation. Our two-stage training paradigm first employs a 3D VQVAE to learn a quantized latent space of multi-scale wavelet features effectively. Second, inspired by VAR [75], we introduce a “token map” prediction paradigm, wherein our AR model predicts entire multi-scale feature maps hierarchically, capturing both global and local details. Wavelet inversion, following the reconstruction of the wavelet representation, yields the final 3D shape at the original implicit resolution. 3D-WAG offers a compelling, efficient alternative to diffusion models, integrating wavelet representations and hierarchical

AR modeling for high-fidelity, controllable, and real-time shape generation.

Our key contributions are:

- ✓ Extending recent advancements in autoregressive generation to direct 3D shape generation with the proposed **3D-WAG** framework, introducing a next-scale prediction strategy for detailed and efficient 3D shape generation.
- ✓ Leveraging compact **wavelet representations** for scalable autoregressive modeling of high-resolution 3D shapes, significantly reducing computational overhead and enabling the use of larger AR architectures.
- ✓ Providing comprehensive experimental validation, demonstrating that **3D-WAG** outperforms existing 3D generative models, including diffusion-based methods, while providing strong generalization in categorical and text-conditioned shape generation.

2 Related Work

Neural networks have revolutionized 3D applications, driving significant progress in shape modeling, scene reconstruction, and virtual simulation [24, 28, 40, 41, 43, 49, 81, 82, 86, 96, 99, 101, 102, 103]. We build upon the established efficacy of neural implicit functions.

2.1 3D Implicit Representations.

Neural Implicit Functions (NIFs) have become indispensable for 3D representation, impacting diverse applications from surface reconstruction [52, 59] to novel view synthesis [53]. Their continuous representation enables high-fidelity rendering and geometry modeling, with advancements ranging from MLP-based SDFs and occupancy fields [52, 59] to neural unsigned distance fields (UDFs) for non-watertight surfaces [8, 13, 43, 44, 79, 98, 100]. However, direct generation with NIFs suffers from a fundamental trade-off: high fidelity necessitates dense sampling and complex networks, leading to significant computational bottlenecks, particularly in AR settings. Recent research leverages compact wavelet-based representations, exploiting signal processing domain knowledge for efficient shape modeling [16, 26, 68, 104]. These representations offer reduced computational effort and maintain detailed latent space information, mitigating compression losses.

In this work, we use compact wavelet-based hierarchical representation that efficiently represents the implicit surface information using lower spatial resolution and increased frequency channels. This transformation reduces the computational burden of 3D convolutions while preserving geometric details, enabling usage of deeper models without parameter overhead (See Table 6 in Appendix). Inherent multi-scale analysis of wavelets aligns perfectly with hierarchical AR modeling, facilitating efficient progressive generation from coarse to fine geometries, a significant advantage over usual direct NIF generation.

2.2 3D Generative Models.

Early 3D generation methods extended image generation techniques like GANs [18], VAEs [31], and flow-based models [32] to 3D, producing point clouds [6, 27, 39, 57, 89] and voxel grids [70, 83]. Recently, diffusion models have emerged as the dominant approach [12, 25, 26, 68, 66, 69, 87]. These models often leverage implicit representations like signed

distance fields (SDFs) [14, 19, 25, 26, 84] or occupancy fields [94] for high-fidelity results, with meshes extracted using marching cubes [45]. To enhance training efficiency, techniques such as Diffusion-SDF [14] and 3D-LDM [65] employ VAEs to transform shapes into latent codes. However, diffusion models face challenges related to training stability and slow inference, limiting their practical applicability [21, 60, 71].

Concurrently, autoregressive (AR) models have shown remarkable progress in 2D image generation [17, 64, 78], and more recently in 3D tasks [11, 64, 66, 72, 80, 88]. A few works explore 3D generation from 2D inputs using AR models; however, they often rely on highly optimized inputs or externally computed 2D feature mappings, limiting real-world applicability [9, 62, 82, 85]. This motivates the need for direct 3D generation using AR methods. Generating high-quality, high-resolution 3D shapes is challenging due to complex representation learning. ShapeFormer [88] adopts a sparse voxel representation quantizing occupied grid cells but uses a fixed row-major order. In contrast, AutoSDF [64] avoids sequential ordering but operates over full volumetric grids, incurring high compute costs. These efforts highlight the trade-off between ordering constraints and efficiency in AR-based 3D generation. For neural implicit functions (NIFs), we propose a paradigm shift from traditional next-token prediction to “next-scale” token map prediction. Conventional AR models struggle with long sequences in dense 3D settings [11, 66, 60, 88]. We address this by using large language models (LLMs) such as GPT-2 [61] to perform both unconditional and conditional generation via simple condition concatenation, enabling faster inference and improved control.

3 Wavelet Autoregressive Shape Generation

Our 3D-WAG employs a wavelet-based representation to compactly represent high-resolution shapes with minimal loss of detail (Sec. 3.1). We follow a two-stage training approach for 3D shape generation. First, a 3D VQVAE autoencoder is trained to encode the wavelet coefficients of 3D shapes into discrete, multi-scale token maps for autoregressive modeling (Sec. 3.2). Subsequently, we use a GPT-2 [61]-like transformer-based autoregressive (AR) model to progressively generate these multi-scale token maps, predicting the next higher-scale token map conditioned on all previous ones (Sec. 3.3). An overview of our complete 3D-WAG framework is provided in Figure 2.

3.1 Compact Wavelet Representations

Modeling high-resolution 3D data in AR settings presents several challenges compared to their 2D image counterparts. The additional third spatial dimension exponentially increases the number of input variables that the model must learn, resulting in a substantial increase in network parameters and memory-intensive feature maps. This added computational overhead on GPUs limits the resolution of 3D shapes that can be modeled and significantly prolongs training and inference times. Moreover, scaling generative models to 3D introduces complex data-handling challenges: the storage and processing of 3D data incur substantially higher I/O costs, such as longer data loading times during each training iteration. Recent methods [25, 26, 68] have leveraged wavelet-based compression techniques to generate high-resolution 3D shapes with diffusion models. Building on these approaches, we adopt a compact wavelet-based spatial frequency representation for efficient signed distance field (SDF) generation in our autoregressive framework.

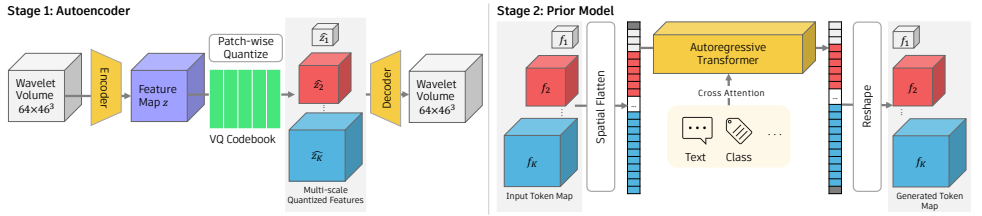


Figure 2: Overview of our architecture. We follow a two-stage training approach that is standard with latent generative models. In Stage 1, we train a vector-quantized autoencoder (VQ-VAE) on the wavelet volumes with multi-scale patch-wise quantization [45] in the latent space giving us quantized feature maps $\hat{z}_1, \hat{z}_2, \dots, \hat{z}_K$. In Stage 2, the multi-scale VQ-VAE codebook indices in the form of token maps f_1, f_2, \dots, f_K are flattened and learned with an autoregressive decoder-only Transformer prior model, enabling next-scale generation. During inference, the generated token maps are reshaped and mapped to obtain multi-scale quantized features by using codebook. Then the obtained features are converted into wavelet volumes by the decoder from Stage 1. The wavelet volumes can be further converted into implicit functions using wavelet inversion.

We first decompose the implicit truncated signed distance field (TSDF) of a 3D shape into multi-scale wavelet coefficients using biorthogonal wavelet transformation, following the previous work [26]. Their selective retention of informative high-frequency detail coefficients ensures fine shape detail preservation with memory efficiency, achieving 99.64 percent IoU concerning input TSDF representation. This enables to use of 3D convolutions with an increased number of channels to learn the shape. Extending beyond watertight meshes, we utilize unsigned distance functions (UDFs) for non-watertight surfaces using the DeepFashion3D dataset. Furthermore, inspired by UDiff [104], we utilize a self-reconstruction process to optimize the parameters of the wavelet filter during both the decomposition and reconstruction phases. Once these wavelet parameters are learned, we use them to create a compact representation of the UDFs consisting of coarse and fine coefficient volumes. We use both of these compact wavelet volumes to represent the 3D shape and showcase the capability of the method in handling the compact wavelet volume input data using our 3D-WAG.

In Table 1, we compare the computational burden, measured in multiply-accumulate operations (MACs), for a single 3D convolution applied to different shape representations using the same kernel. The results show that the wavelet-based representation is significantly more efficient than the implicit representation at the same voxel resolution. Additional details on the compact wavelet input are provided in Appendix 6.

Table 1: **MACs of 3D convolutions on implicit and wavelet representations.** Wavelet representation reduces MACs by $\sim 3\times$.

Representation	Ch.	Filter	MACs
Implicit (1×256^3)	1	3^3	453M
Wavelet (64×46^3)	64	3^3	168M

3.2 Multi-Scale Wavelet Tokenization

To facilitate generative autoregressive (AR) modeling via next-token prediction, it is imperative to first translate each data instance into a sequence of discrete tokens by tokenization. Subsequently, a specific one-dimensional (1D) ordering of these tokens must be established,

enabling the model to learn a unidirectional predictive pattern. Predicting each token conditioned on its predecessors allows for coherent and context-aware generation. However, for the non-sequential data, such as 3D shapes, the direct flattening of spatial features into linear sequences for autoregressive modeling can disrupt the inherent spatial structure. This naïve flattening approach weakens the natural correlations between the distant features, effectively disregarding the original spatial relationships.

To mitigate these limitations, we formulate 3D shape generation as a hierarchical feature prediction task [14], wherein the model estimates wavelet token maps instead of individual tokens at progressively higher resolutions. To enable this multi-scale generation process, we train an autoencoder, 3D VQVAE that encodes each 3D shape into K discrete token maps spanning varying resolutions or scales. This multi-scale discretization allows for the representation of shapes at different levels of detail, ranging from coarse structural information in low-resolution token maps to fine geometric details in high-resolution ones.

For each shape S , an autoencoder 3D VQVAE learns to compress continuous wavelet coefficients W into multi-scale discrete token maps $F = (f_1, f_2, \dots, f_K)$, where f_1 and f_K are the coarsest and finest scales, respectively. Using a 3D convolutional VAE with a modified multi-scale quantization layer, inspired by [36, 14], we quantize each f_k conditioned on $(f_1, f_2, \dots, f_{k-1})$ with a shared codebook Z . This enables progressive, coherent multi-scale reconstruction, preserving details for autoregressive generation. The multi-scale encoding and reconstruction steps of 3D VQVAE are detailed in stage 1 in Figure 2.

3.2.1 Multi-Scale Encoding

The multi-scale vector quantization encoding scheme progressively encodes an input shape representation W across multiple resolutions, utilizing residual connections to capture details at varying scales (Stage 1 of Figure 2). Given a wavelet input W , an encoder E generates an initial feature map z . This map is then iteratively quantized over K steps, each corresponding to a predefined resolution (h_k, w_k, d_k) . At each scale k , the current residual tensor z_k^{res} is interpolated to match (h_k, w_k, d_k) . At the finest scale K , z_K^{res} is initialized with z . The interpolated tensors are quantized using the method from [36, 14] to obtain token maps f_k from codebook Z , which stores learned feature vectors with indices. These maps retrieve feature vectors from Z , creating a quantized representation \hat{z}_k^{res} . At scale k , \hat{z}_k^{res} serves as an estimate of z_k^{res} . Subsequently, \hat{z}_k^{res} is upsampled to the original scale. A residual is computed by subtracting $C_k(\hat{z}_k^{res})$ from z_k^{res} , yielding z_{k-1}^{res} . This process is repeated for all scales. Here, C_k is a convolutional layer at scale k , mitigating information loss during upscaling. Notably, convolutional layers are omitted during downsampling of z . This recursive process generates a sequence of multi-scale tokens F , encapsulating hierarchical and multi-resolution information from the wavelet encodings.

3.2.2 Multi-Scale Reconstruction

The multi-scale reconstruction scheme reverses the encoding process, reconstructing a wavelet representation from the multi-scale token maps generated during encoding. Given a sequence of multi-scale token maps F , the scheme iteratively reconstructs a feature map \hat{z}^{recon} by decoding information at progressively finer scales. The process begins by initializing \hat{z}^{recon} to zero. For each scale k in the sequence of K steps, we retrieve the quantized representation f_k from F . Then, uses a codebook (Z) lookup to obtain a latent representation z_k^{recon} , corresponding to the token map f_k . This latent representation z_k^{recon} is interpolated to match the

current resolution (h_k, w_k, d_k) . A residual connection is employed, where the current estimate \hat{z}^{recon} is updated by adding $C_k(\hat{z}_k^{recon})$. Once all scales are processed, a decoder D is applied to \hat{z}^{recon} to reconstruct the final wavelet volume \hat{W} .

The autoencoder is trained by minimizing a composite loss that encourages accurate reconstruction, latent consistency, and fine-detail preservation. The objective includes three terms: (i) a reconstruction loss between the original wavelet representation W and its reconstruction \hat{W} , (ii) a commitment loss that encourages the encoder to map consistently to discrete embeddings across K scales, and (iii) a detail-aware loss detailed in Sec. 3.2.3 focusing on high-frequency coefficients. The overall training objective is:

$$L = \lambda_{\text{recon}} \|W - \hat{W}\|_2 + \lambda_{\text{commit}} \sum_{k=1}^K \|\hat{z}_k^{\text{res}} - z_k^{\text{res}}\|_2 + \lambda_{\text{detail}} L_{\text{detail}}, \quad (1)$$

where λ_{recon} , λ_{commit} , and λ_{detail} are weighting hyperparameters.

3.2.3 Detail Loss

To improve the fidelity of 3D shape reconstruction, especially around fine-grained geometric features we utilize a **detail-aware loss** that focuses specifically on high-frequency components of the wavelet representation. This loss selectively penalizes reconstruction errors at spatial locations identified as containing meaningful high-frequency information. Let $\mathcal{M}_b \subseteq \Omega$ denote the set of valid high-frequency spatial indices for sample b , determined by a binary mask, and let C be the number of channels. The detail loss measures squared error between the predicted and ground truth wavelet coefficients at these high-frequency locations, averaged across channels and samples in a batch of size B :

$$L_{\text{detail}} = \frac{1}{B} \sum_{b=1}^B \left[\frac{1}{C} \sum_{c=1}^C \left(\frac{1}{|\mathcal{M}_b|} \sum_{i \in \mathcal{M}_b} \left(W_{b,i}^{(c)} - \hat{W}_{b,i}^{(c)} \right)^2 \right) \right], \quad (2)$$

where $W_{b,i}^{(c)}$ and $\hat{W}_{b,i}^{(c)}$ denote the ground truth and predicted wavelet coefficients at spatial index i , channel c , and sample b . By explicitly encouraging accurate reconstruction of high-frequency details, 3DWAG ensures that the model captures fine surface structure more precisely, enabling high-fidelity modeling of wavelet-encoded 3D data.

3.3 Next-Scale Token Map Prediction using AR

The multi-scale token map feature encodings, learned during the first stage of training, are used to train an autoregressive shape generation model. The weights of 3D VQVAE during the second stage of training are frozen. In the second stage, the goal of the AR Transformer model is to generate token maps $\{f_1, f_2, \dots, f_K\}$ using a "next-scale prediction" approach (Stage 2 part of Figure 2). Starting with a random initial token map, the model generates subsequent token maps one step at a time, each at progressively higher resolutions. This process continues until it reaches f_K , which matches the resolution of the original feature map. To accomplish this, we utilize a GPT-2 [61] style decoder-only Transformer model. The AR likelihood is defined as: $p(f_1, f_2, \dots, f_K) = \prod_{i=1}^K p(f_i | f_{<i})$, where each f_i is conditioned on all preceding token maps $f_{<i}$. It is important to note that, at each step, all token maps at the **current** scale are estimated simultaneously rather than sequentially. For class-conditional synthesis, we use a class embedding as the start token, denoted by $[s]$, which also serves as

the conditioning factor for network AdaLN. Additionally, we normalize the queries and keys to unit vectors before the attention mechanism, enhancing training stability in our generative model. The cross-entropy loss L_{CE} is employed for AR shape generation:

$$L_{CE} = - \sum_{i=1}^K \log p(f_i | f_{<i}), \quad (3)$$

where $p(f_i | f_{<i})$ is the predicted probability of the i -th token map f_i given all previous token maps $f_{<i}$. This loss function encourages the model to assign high probabilities to the correct token map f_i at each step, ensuring detail oriented autoregressive generation by minimizing the negative log-likelihood of the true token maps. During autoregressive inference, multi-scale token maps are sampled progressively, capturing spatial details at increasing resolutions. This sequential process enables the model to coherently generate complex shapes, refining details at each scale to produce a realistic output. These token maps are transformed into a wavelet reconstruction \hat{W} using the **Reconstruction** algorithm presented in Sec. 3.2.

The wavelet representation is inverted using an inverse wavelet transform to generate an implicit representation of the shape. Additional design choices and implementation details of shape retrieval from the wavelet representation are given in Appendix 7, 8, 9. We also note that, in the 3D case, generating a volume token sequence $\{f_1, f_2, \dots, f_K\}$ with a conventional self-attention Transformer requires $\mathcal{O}(n^3)$ autoregressive steps and incurs a computational cost of $\mathcal{O}(n^9)$. By employing the 3D-WAG approach, the time complexity for an $n \times n \times n$ latent representation is substantially reduced to $\mathcal{O}(n^6)$, see Appendix 10 for the proof.

4 Experiments

4.1 Dataset and Metrics

We evaluate our method on DeepFashion3D [105] (1,798 garments, 563 items, 10 categories) and ShapeNet [6] (51,300 models, 55 categories), using 80/20 train/test splits. Shapes are represented as signed (ShapeNet) or unsigned (DeepFashion3D) distance fields at 256^3 resolution. Unconditional generation performance is assessed via Coverage (COV), Minimum Matching Distance (MMD), and 1-Nearest Neighbor Classifier Accuracy (1-NNA), generating 1000 (DeepFashion3D) and 2000 (ShapeNet) samples with 2048 points sampled from the surfaces. For ShapeNet, quantitative metrics are reported on airplane and chair categories, following [25, 32], while qualitative evaluations utilize the entire dataset. We argue that our model can also be used on other 3D datasets; however, due to limited computing resources, we restrict our evaluations to the mentioned datasets. In Appendix 13, we further provide an ablation on our design choices.

4.2 Results on ShapeNet

We present our results on ShapeNet dataset in Table 2. We compare our 3D-WAG model to previous methods, including UDiFF [104], IM-GAN [10], Voxel-GAN [33], PointDiff [46], SPAGHETTI [70], WaveGen [25], and SALAD [32]. We also evaluate our approach in comparison to the autoregressive approach ImAM [47], which uses token-by-token prediction to generate shapes. Our model improves over these previous models.

Specifically, we obtain improved COV and MMD across the Chair and Airplane categories. The high COV reflects the model’s ability to generate diverse, realistic shapes, while

Table 2: **Shape generation performance and time on ShapeNet.** Inference time is in seconds on A6000. MMD-CD and MMD-EMD scores are scaled by 10^3 and 10^2 , respectively.

Method	COV \uparrow		Chair MMD \downarrow		1-NNA \downarrow		COV \uparrow		Airplane MMD \downarrow		1-NNA \downarrow		Time (s)
	CD	EMD	CD	EMD	CD	EMD	CD	EMD	CD	EMD	CD	EMD	
IM-GAN [10]	57.01	55.23	12.02	14.76	62.15	63.78	62.21	63.10	3.298	8.479	76.50	76.29	2.98
Voxel-GAN [11]	44.29	39.89	15.35	17.59	80.74	81.62	39.01	39.78	5.875	11.53	93.60	92.98	2.75
PointDiff [12]	51.88	56.11	12.92	16.35	62.02	63.95	60.55	62.71	3.615	9.620	74.98	72.63	–
SPAGHETTI [13]	50.11	50.73	15.02	16.05	72.82	69.93	57.30	59.12	4.342	9.021	79.84	79.33	27.4
SALAD (Global) [14]	50.13	49.12	11.93	14.35	63.25	61.73	55.42	59.85	3.891	9.073	82.61	80.87	33.2
SALAD [14]	56.91	55.65	11.89	14.50	58.23	58.90	63.65	65.82	3.721	8.329	74.35	71.52	38.0
WaveGen [15]	50.12	50.67	12.31	14.47	65.58	63.39	61.40	59.57	3.605	8.075	76.23	73.25	15.4
ImAM [16]	54.38	55.71	11.90	13.97	62.43	62.11	65.82	65.41	3.248	7.900	77.12	79.13	14.2
UDiff [17]	53.02	56.51	11.82	14.19	66.42	63.91	65.23	64.22	3.229	7.879	74.85	79.42	39.0
Ours	57.30	58.41	10.90	13.06	68.10	66.31	66.80	65.93	2.900	7.543	82.10	80.92	2.50

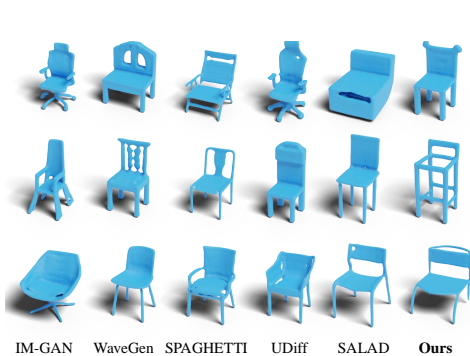


Figure 3: 3D chair generation results on ShapeNet, comparing IM-GAN, WaveGen, SPAGHETTI, UDiff, and SALAD, with our 3D-WAG on the far right. 3D-WAG shows improved structural coherence, finer details, and a wider diversity of generated designs, capturing both simple and complex geometries more effectively than other methods.

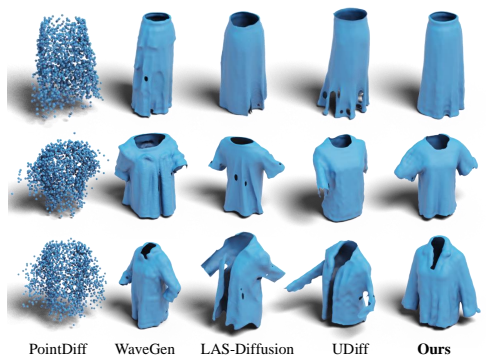


Figure 4: 3D garment generation results on the DeepFashion3D dataset [18], comparing PointDiff, WaveGen, LAS-Diffusion, UDiff, and our method (3D-WAG) on the far right. 3D-WAG produces more coherent and realistic garment shapes, capturing intricate structural details such as folds, sleeves, and openings with higher fidelity than other methods.

the low MMD indicates strong fidelity to the real data distribution, confirming the benefit of our autoregressive next-scale token map prediction strategy in capturing high-resolution geometric details without significant computational overhead. The slightly higher 1-NNA arises from our focus on preserving fine-grained local details, which, while enhancing geometric precision, can lead to sharper features that nearest neighbor classifiers more readily detect. This trade-off reflects our design choice to prioritize high-quality, detailed shape generation over smoothing, which may lower 1-NNA at the expense of visual and structural richness. Overall, these results demonstrate the effectiveness of 3D-WAG in jointly improving diversity, fidelity, and inference efficiency in 3D shape generation. Qualitative comparisons in Fig. 3 further highlight the superior detail and variety achieved by our method.

4.3 Results on DeepFashion3D

We compare our approach with SOTA diffusion-based generation approaches, including UDiff [102], PointDiff [46], WaveGen [25], Diffusion-SDF [4], and LAS-Diffusion [97]. Each model is evaluated with the official implementations. WaveGen [25] and UDiff [102] are also based on wavelet input representation, ensuring a fair comparison.

Table 3 highlights the superior performance of 3D-WAG on the DeepFashion3D dataset compared to previous approaches. 3D-WAG achieves the highest Coverage (COV) scores, with 69.85 (CD) and 68.03 (EMD), indicating a broader diversity of generated shapes that better represent the dataset’s range of 3D garments. Additionally, 3D-WAG excels in Minimum Matching Distance (MMD), achieving the lowest scores across both CD and EMD metrics, with values of 10.96 and 13.89, respectively, demonstrating higher fidelity to real shapes. The 1-Nearest Neighbor Accuracy (1-NNA) scores of 82.01 (CD) and 82.30 (EMD) further confirm that 3D-WAG produces realistic samples with a similarity distribution close to the real data. These results validate the effectiveness of our approach in open-surface shape generation in terms of both diversity and quality. Fig. 4 presents qualitative examples of our unconditional generation results on DeepFashion3D. More unconditional generation results, including failure cases and conditional generation, are found in Appendix 11 12 14.

Table 3: **Shape generation on DeepFashion3D.** MMD-CD and MMD-EMD scores are scaled by 10^3 and 10^2 , respectively.

Method	COV \uparrow		MMD \downarrow		1-NNA \downarrow	
	CD	EMD	CD	EMD	CD	EMD
PointDiff [46]	68.90	64.89	11.20	15.72	83.50	87.93
WaveGen [25]	62.75	52.15	15.78	17.29	93.20	94.96
Diffusion-SDF [4]	67.45	62.40	14.92	16.88	89.31	92.81
LAS-Diffusion [97]	67.82	56.43	14.75	16.79	88.95	91.68
UDiff [102]	69.98	68.01	11.75	14.25	82.11	82.47
Ours	69.85	68.03	10.96	13.89	82.01	82.30

5 Conclusion

We present 3D-WAG, a novel autoregressive approach for 3D shape generation that operates directly on 3D representations. 3D-WAG transforms the traditional "next-token" prediction framework of 3D autoregressive methods to a "next-scale token map" prediction framework. The key innovation of 3D-WAG is reframing 3D autoregressive generation as a "next-scale token map" prediction task using a compact wavelet representation as input, enabling efficient generation while preserving intricate geometric details in a structured, hierarchical way. This approach is validated by 3D-WAG’s outstanding performance on widely recognized benchmarks, where it achieves superior Coverage and MMD metrics compared to SOTA models. Our results show that 3D-WAG generates high-fidelity 3D shapes that are closely aligned with real data distributions, while requiring less inference time.

Future Work While this work primarily introduces a novel and competitive approach to 3D shape generation, we plan to further optimize the autoregressive generation module. Additionally, we aim to explore a broader range of applications, potentially enabling more complex 3D generation scenarios. Furthermore, we will investigate alternative conditioning mechanisms to enhance the flexibility and robustness of 3D-WAG across diverse 3D tasks.

Appendix: Supplementary Material

The supplementary material provides additional details of our approach, **3D-WAG**. The Appendix is organized as follows:

- ✓ **Input Compact Wavelet Representation:** Section 6 discusses the wavelet input representation details utilized in our approach.
- ✓ **Architectural Details:** Section 7 describes the architectural details of our approach.
- ✓ **Implementation Details:** Section 8 provides the implementation details and the hyperparameters of our approach.
- ✓ **Wavelet Inversion for 3D Mesh Extraction:** Section 9 discusses the details of extraction of 3D meshes from compact wavelet representations.
- ✓ **Time Complexity Analysis:** Section 10 presents insights into the time-complexity analysis of our approach.
- ✓ **Additional Results:** Section 11 showcases more results demonstrating the performance of our approach.
- ✓ **Failure Cases:** Section 12 highlights the failure cases observed in our approach.
- ✓ **Ablation Studies** Section 13 presents the ablations on key components of our generation process.
- ✓ **Conditional Generation:** Section 14 explores the class and text conditional generation capabilities of 3DWAG.

6 Input Compact Wavelet Representation

In our approach, we use compact wavelet representations as input to define the truncated signed distance function (TSDF) and the Unsigned distance function (UDF) of a 3D shape. We use the optimal wavelet strategy for both SDF and UDF from [26] and [102], respectively.

6.1 SDF-Compact Wavelet Representation

Following [26], we first decompose a truncated signed distance function (TSDF) of a 3D shape at a resolution of 256^3 using biorthogonal wavelet transformations with 6 and 8 moments. The choice of this wavelet filter is from [25]. This decomposition produces a hierarchical representation consisting of a coarse component (low-frequency information) and a set of seven detail components (high-frequency information) for each decomposition level.

At the initial decomposition level ($\ell = 2$), the input TSDF is decomposed into a coarse component C_2 and a set of seven detail components $\{D_2^{(i)}\}_{i=1}^7$. This process continues recursively, where at each level $\ell - 1$, the coarse component C_ℓ is further decomposed into a lower-resolution coarse component $C_{\ell-1}$ (capturing the global shape structure) and a set of seven detail components $\{D_{\ell-1}^{(i)}\}_{i=1}^7$ (capturing finer details). This can be expressed mathematically as follows:

$$C_\ell \rightarrow \left\{ C_{\ell-1}, D_{\ell-1}^{(1)}, D_{\ell-1}^{(2)}, \dots, D_{\ell-1}^{(7)} \right\}, \quad (4)$$

Each coarse component serves as a *parent*, while its corresponding detail components act as *children*. This parent-child relationship is not restricted to coarse-detail interactions; it also extends across different decomposition levels, where detail components at level $\ell - 1$ influence those at level ℓ as they are used in reconstructing the coarse component at level $\ell - 1$. Thus, the wavelet decomposition can be naturally represented as a wavelet tree representation as mentioned in [26].

The structured wavelet tree decomposition enables efficient multi-scale shape representations and facilitates hierarchical processing. We use subband coefficient filtering and subband coefficient packing from [26] to locate and pack the information-rich coefficients in building our compact wavelet representation by ignoring the coefficients that make a very low contribution or no contribution to the shape. By ignoring these information-lacking coefficients, we obtain a compact wavelet volume.

6.2 UDF-Compact Wavelet Representation

For compact wavelet representation based on UDF, we follow the data-driven approach to learn the optimal wavelet transformation for UDFs, aiming to minimize information loss during compression and reconstruction following [102]. Inspired by [104], we learn a biorthogonal wavelet filter, comprising a decomposition filter ϕ_θ^D and an inversion filter ϕ_δ^I with learnable parameters θ and δ , respectively.

Given a set of shapes $S_{i=1}^N$, we sample the UDF volume U_i for each shape at a resolution of 256^3 , truncate the distance values to $[0, 0.1]$, and compress it into a coarse coefficient volume C_i and a detail coefficient volume D_i using ϕ_θ^D : $C_i, D_i = \phi_\theta^D(U_i)$. Then, we reconstruct a lossy UDF \hat{U}_i from C_i and D_i using ϕ_δ^I : $\hat{U}_i = \phi_\delta^I(C_i, D_i)$. The filter parameters are optimized by minimizing the mean squared error (MSE) between the original and reconstructed UDFs, with weights w_i^γ emphasizing the region near the zero-level set (where γ is a threshold parameter): $\min_{\theta, \delta} \sum_{i=1}^N \mathcal{L}_{MSE}(w_i^\gamma \hat{U}_i, w_i^\gamma U_i)$. This data-driven optimization yields an optimal wavelet transform that faithfully reconstructs the original UDF while remaining compact. All the hyperparameters are the same as mentioned in [104].

7 Architectural Details

The architecture of 3D-WAG draws inspiration from VAR [75], which has demonstrated superior performance compared to diffusion models in 2D image generation. In this work, we adapt the VAR framework to generate 3D shapes by modeling auto-regression as a coarse-to-fine detail prediction process. This is achieved by leveraging spatial frequency features extracted from the wavelet-based compact data representation of 3D shapes. To accommodate the 3D setting and wavelet-based input representation, the 3D-WAG architecture is extended and modified accordingly. Detailed information about the 3D-WAG architecture is provided below.

Stage 1: Autoencoder

The first stage of 3D-WAG involves training a U-Net-based autoencoder similar to the VQGAN framework [17]. We extend the U-Net architecture to process 3D data by replacing

Table 4: Encoder Architecture: Processes input features using 3D convolutions, residual blocks, and optional attention mechanisms, followed by downsampling to obtain a compact latent representation.

Encoder Stage	Operation	Output Dimensions
Input	-	$\mathbb{R}^{B \times C_{\text{in}} \times H \times W \times D}$
Initial Convolution	Conv3D($C_{\text{in}}, C, 3, 1, 1$)	$\mathbb{R}^{B \times C \times H \times W \times D}$
Downsampling	For $i = 1, \dots, L$:	
Residual Block	ResNetBlock($C_{\text{in}}, C_{\text{out}}$)	$\mathbb{R}^{B \times C_{\text{out}} \times H \times W \times D}$
Attention Block	AttnBlock(C_{out})	Same as above
Downsample	Downsample2x	$\mathbb{R}^{B \times C_{\text{out}} \times \frac{H}{2} \times \frac{W}{2} \times \frac{D}{2}}$
Middle Layers	-	
Residual Block	ResNetBlock(C, C)	$\mathbb{R}^{B \times C \times \frac{H}{2^{L-1}} \times \frac{W}{2^{L-1}} \times \frac{D}{2^{L-1}}}$
Attention Block	AttnBlock(C)	Same as above
Residual Block	ResNetBlock(C, C)	Same as above
Output Convolution	Conv3D($C, C_z, 3, 1, 1$)	$\mathbb{R}^{B \times C_z \times \frac{H}{2^{L-1}} \times \frac{W}{2^{L-1}} \times \frac{D}{2^{L-1}}}$
Output	-	Same as above

its 2D CNN layers with 3D CNNs, enabling efficient handling of volumetric wavelet features. To reconstruct or learn the wavelet-transformed inputs, which provide richer channel information at a lower volumetric spatial resolution, we modify the compression ratio of the architecture and adjust the dimensionality of the latent compact features. This adaptation yields a continuous latent representation with a channel dimensionality of 512 with a spatial resolution of 11^3 , optimized to capture both low and high-frequency components of 3D wavelet data effectively.

The Encoder and Decoder of 3D-WAG utilize 3D convolutional blocks, as detailed in Tables 4 and 5. The number of downsampling or compression levels, L , in the encoder and decoder stages is set to either 2 or 3, depending on the dataset size. For datasets with fewer samples, compression is reduced to better preserve distinguishing features between samples. In Table 4 and 5, C_{in} and C_{out} represent the input and output channel dimensions, respectively, while H , W , and D denote the height, width, and depth of the input compact wavelet volume data. C_z , corresponds to the channel dimension of the compact global feature map z .

Multi-Scale Quantization: In our approach, we adopt a multi-scale quantization scheme similar to the one proposed in [45] for 2D data, instead of directly quantizing the global latent feature map z into tokens. Specifically, the continuous global feature map z is quantized into K multi-scale discrete token maps, denoted as $\{f_1, f_2, \dots, f_K\}$, where the highest resolution is represented by f_K . Each token map f_k has a resolution of (H_k, W_k, D_k) . To ensure consistency across scales, a shared codebook Z is utilized for quantization, such that the token maps at each scale f_k belong to the same vocabulary defined by Z . To address potential information loss when upsampling the lower-resolution latent feature maps f_k to the highest resolution (H_k, W_k, D_k) , we introduce $K - 1$ additional convolution layers, $\{C_j\}_{j=1}^{K-1}$. These layers refine the upscaled features to recover detailed information. These multi-scale token maps are important in modeling the generation of shapes. Higher-resolution token maps can

Table 5: Decoder Architecture: Reverses the encoder operations by progressively upsampling latent features to reconstruct the input dimensions.

Decoder Stage	Operation	Output Dimensions
Input	-	$\mathbb{R}^{B \times C_z \times \frac{H}{2^{L-1}} \times \frac{W}{2^{L-1}} \times \frac{D}{2^{L-1}}}$
Initial Convolution	Conv3D($C_z, C, 3, 1, 1$)	$\mathbb{R}^{B \times C \times \frac{H}{2^{L-1}} \times \frac{W}{2^{L-1}} \times \frac{D}{2^{L-1}}}$
Middle Layers	-	-
Residual Block	ResNetBlock(C, C)	Same as above
Attention Block	AttnBlock(C)	Same as above
Residual Block	ResNetBlock(C, C)	Same as above
Upsampling	For $i = L, \dots, 1$:	-
Residual Block	ResNetBlock(C_{in}, C_{out})	$\mathbb{R}^{B \times C_{out} \times \frac{H}{2^{L-1}} \times \frac{W}{2^{L-1}} \times \frac{D}{2^{L-1}}}$
Attention Block	AttnBlock(C_{out})	Same as above
Upsample	Upsample2x	$\mathbb{R}^{B \times C_{out} \times 2H \times 2W \times 2D}$
Output Convolution	Conv3D($C, C_{out}, 3, 1, 1$)	$\mathbb{R}^{B \times C_{out} \times H \times W \times D}$
Output	-	Same as above

be predicted from lower-resolution ones, facilitating a coarse-to-fine generation process.

Stage 2: Prior Model

We employ the GPT-2 decoder-only transformer model [60] to model auto-regressive shape generation, leveraging its demonstrated ability to generate high-resolution token maps from low-resolution token maps in image generation [75]. In this work, we adopt the same architecture to produce fine details from high-resolution token maps starting from coarser, lower-resolution token maps. To achieve this, we first flatten the multi-scale token maps, $\{f_1, f_2, \dots, f_K\}$, at each scale. Specifically, these token maps, originally defined with dimensions (B, C_z, H_k, W_k, D_k) , where $k \in \{1, 2, 3, \dots, K\}$, are transformed into a sequence of token maps with dimensions (B, C_z, S_k) , where $S_k = H_k \times W_k \times D_k$ represents the spatial size of the token map at scale k , B is batch size and C_z represents the channel dimensionality of the token map. The decoder-only transformer network is then utilized to predict the token map at a higher scale based on the token map at a lower scale. This auto-regressive generation process is performed iteratively over the token maps, progressively enabling the model to generate shapes from coarse to fine resolution details.

8 Implementation Details

We outline the implementation details and hyperparameters used in our approach. The training was conducted on two types of GPUs: 4 NVIDIA H100 GPUs with 93.58 GB of VRAM each and 4 NVIDIA A6000 GPUs with 47.55 GB of VRAM each. In the first stage, during training, we used 11 scales of quantization, which means 11 token maps are learned to model the second stage of the 3D-WAG generation process. The codebook size (Z) was set to 8192 for the DeepFashion3D and ShapeNet subset datasets, while for the full ShapeNet dataset, it

was increased to $Z = 16384$. The model was trained with a learning rate of 1×10^{-4} and a batch size of 48 on 4 GPUs in parallel. The loss weights for λ_{recon} , λ_{commit} , and λ_{detail} is set to 1.

For the Signed Distance Fields (SDF), we used a wavelet-based input representation with dimensions $(1, 64, 46, 46, 46)$, following the design in [68]. For the Unsigned Distance Fields (UDF), we adopted the representation proposed in [104], where the low-frequency wavelet components are represented at a resolution of 46^3 , and the high-frequency wavelet components are represented at a resolution of 76^3 . These components are fused using a learnable layer, resulting in a compact wavelet representation with a resolution of 46^3 . This fusion retains high-frequency information while ensuring compatibility with our approach, which expects 46^3 spatial resolution. For stage-2 prior model training, we use the same hyperparameter setting as in VAR [75] with an embedding dimension of 8192. We trained stage 1 of 3DWAG for 150 epochs, and for stage 2, we trained for 250 epochs.

9 Wavelet Inversion

As discussed, we employ the compact wavelet-based input representation from recent works [68, 104] to represent Signed Distance Fields (SDF) and the Unsigned Distance Fields (UDF), respectively. We utilize the same implicit function extraction techniques outlined in [68] and [104] for generating the respective implicit representations from compact wavelet data. In the case of SDF-based compact wavelet representation, we use the coarse and detail coefficients of the compact wavelet volume generated by the decoder to reconstruct the SDF using biorthogonal wavelet filter inversion. In the case of UDF-based wavelet representation, we use an inversion filter learned to reconstruct the UDF from the generated wavelet coefficient volume. Later, we use marching cubes in case of extracting the surfaces from SDF and DCUDF [23] to extract the surface from UDF, ensuring a fair comparison with prior works.

10 Time Complexity of 3D-WAG Generation

In this section, we compare the time complexity of a standard autoregressive (AR) model with that of our proposed 3D-WAG approach. While AR models incur high computational costs due to their quadratic scaling in self-attention, 3D-WAG reduces complexity by employing a progressive resolution strategy. Below, we derive the time complexities of both methods. We refer to [75] for the image analog of this derivation.

AR generation complexity For a standard AR model, implemented with a self-attention transformer, the time complexity is $\mathcal{O}(n^9)$ for generating a volume of size $x \times y \times z = n^3$ (assuming $x = y = z = n$).

Proof: At each iteration $1 \leq i \leq n^3$, the model performs $\mathcal{O}(i^2)$ computations due to the quadratic scaling of self-attention with the number of tokens. The total time complexity is therefore:

$$\sum_{i=1}^{n^3} i^2 = \frac{n^3(n^3+1)(2n^3+1)}{6} \sim n^9 \quad (5)$$

3D-WAG complexity. In contrast, 3D-WAG generates volumes autoregressively at progressively increasing resolutions. Specifically, the generated volumes have sizes $(x_1, y_1, z_1), (x_2, y_2, z_2), \dots$ which we assume satisfy $x_k = y_k = z_k = n_k$. In our experiments, the resolution n_k grows sub-linearly with the step index k , and we parameterize this growth as $n_k = a^{k-1}$, where $a > 1$.

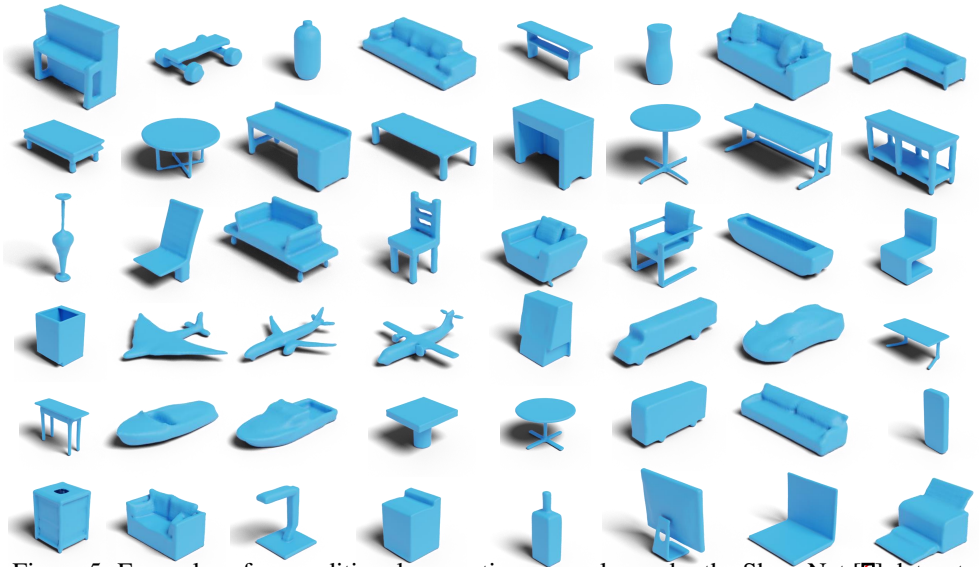


Figure 5: Examples of unconditional generation examples under the ShapeNet [14] dataset.

This progressive resolution strategy significantly reduces the computational cost, achieving a time complexity of $\mathcal{O}(n^6)$, as shown below.

Proof: The total number of tokens up to step k is given by the geometric sum:

$$\sum_{i=1}^k n_i^3 = \sum_{i=1}^k a^{3(i-1)} = \frac{1 - a^{3k}}{1 - a^3} \quad (6)$$

The computational complexity of generating all tokens up to step k is proportional to the square of this quantity, since at each step the attention mechanism operates on all previously generated tokens. Thus:

$$\text{Time complexity} \sim \sum_{k=1}^K \left(\frac{1 - a^{3k}}{1 - a^3} \right)^2 \quad (7)$$

The dominant term in the geometric sum is a^{3k} , and so:

$$\sum_{k=1}^K \left(\frac{1 - a^{3k}}{1 - a^3} \right)^2 \sim \sum_{k=1}^K a^{6k} \sim a^{6K} \quad (8)$$

Using $K = \log_a(n) + 1$ (where n is the resolution of the final volume), it follows that the total time complexity is $\mathcal{O}(n^6)$.

11 Additional Results

In this section, we present additional results generated by 3D-WAG.

Unconditional Generation: Figure 5 showcases examples from the unconditional generation setting. The model was trained on the entire ShapeNet dataset, consisting of approximately 55000 samples. The results highlight the diversity of the generated shapes and their consistency with the characteristics of the training data.

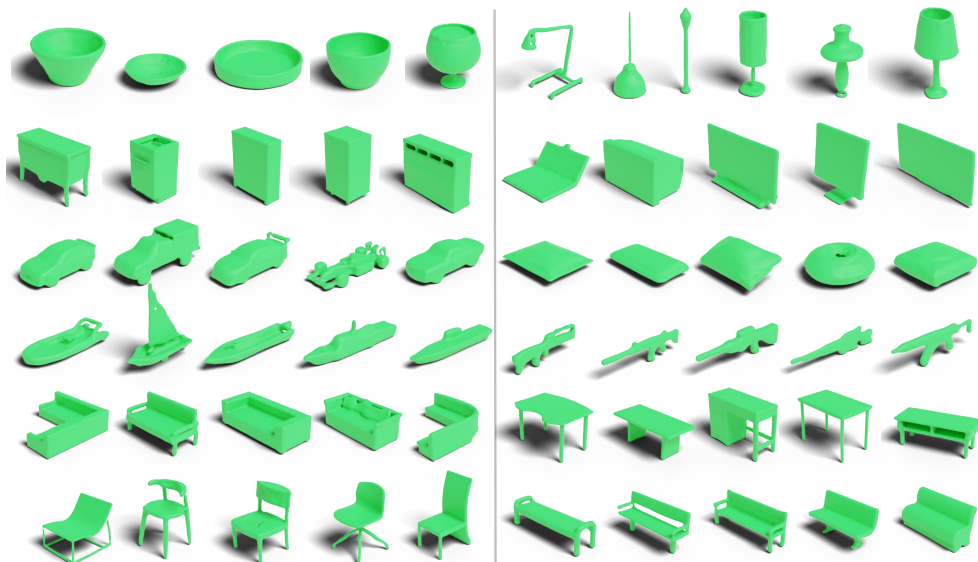


Figure 6: Class-conditional generation results on the ShapeNet [10] dataset. Twelve categories are illustrated, with two categories per row. Categories from left to right, top to bottom, are: Bowl, Lamp; Cabinet, Monitor; Car, Pillow; Watercraft, Rifle; Sofa, Table; Chair, Bench. Each category showcases the diversity of shapes generated within its class.

Class-Conditional Generation: Additional examples of conditional generation are provided in Figure 6. For these results, the model was trained on a subset of ShapeNet containing 15 classes, using class labels as conditioning inputs. These results demonstrate the model’s ability to adaptively generate shapes based on the provided class labels.

12 Failure Cases



Figure 7: Examples of failure cases produced by 3D-WAG. On the left, we show samples from the unconditional generation setting, where shapes exhibit a lack of clear semantic meaning (first shape), incomplete details (missing legs of the chair), or artifacts (holes in the table). On the right, in the text-to-3D generation task, the produced shapes fail to fully capture the prompt information, as the dress has one sleeve.

Our model occasionally generates shapes with incomplete details or unclear semantic meaning in the generation setting. We show examples of this behavior in Figure 7 (left).

In the text-to-3D generation scenario, the output may fail to fully represent the prompt’s specifications, as illustrated in Figure 7 (right). These limitations can be attributed to the relatively small size of the datasets. Specifically, the datasets used for text-to-3D generation were particularly limited, while ShapeNet [6] and DeepFashion3D [105], containing about 55000 and 1798 samples respectively, are not considered large-scale datasets. We hypothesize that scaling our approach to larger datasets could significantly reduce the frequency of such failure cases, consistent with findings in prior studies on similar tasks [29].

13 Ablation Studies

In the following, we examine the influence of several key components in our generation process:

- **Compact Wavelet Representations:** We evaluate the benefits of using compact wavelet representations vs direct implicit 3D representation.
- **Codebook Size:** We first investigate how varying the size of the codebook affects the reconstruction performance of 3DWAG.
- **Number of Token Maps / Stages:** We analyze the effect of varying the number of token maps in generation process.
- **Quantization Techniques:** Finally, we explore different quantization methods to understand their impact on the generation process.

Ablation on the Compact Wavelet Representation To address the limitations of autoregressive (AR) models in 3D shape generation, we propose 3D Hierarchical Wavelet-Guided Autoregressive Generation (3D-WAG), leveraging compact hierarchical wavelet representations, which are recently also being used in diffusion based generation models [68, 104]. We showcase effectiveness of using wavelet representation over using implicit representation directly in Table 6.

Table 6: Comparison of wavelet vs. direct implicit 3D representations for AR modeling using 3D VQVAE at 256³ resolution on DeepFashion3D dataset with 3D-WAG. Metrics computed using Chamfer Distance.

Params	Rep.	MMD ↓	COV ↑	1-NNA ↓
115M	Imp.	—	—	—
	Wav.	11.03	68.98	82.23
60M	Imp.	15.98	58.32	87.56
	Wav.	13.72	63.44	84.09

Ablation Study on Codebook Size To analyze the impact of codebook size on the reconstruction performance of our proposed 3D-WAG approach, we conducted an ablation study. Specifically, we evaluated the reconstruction error between the input wavelet volume data and the predicted wavelet data from the validation set of the ShapeNet dataset, which includes 55 categories.

Table 7 summarizes the results of reconstruction loss evaluated using mean square error loss between the input and predictions by our approach. The findings indicate that a larger codebook size is advantageous as it provides greater diversity by accommodating more shape information and therefore improves reconstruction performance.

Table 7: Reconstruction error for different codebook sizes.

Codebook Size	Reconstruction Error
8192	0.00005
16,384	0.00002

Table 8: **Shape generation on the planes dataset. Ablation on the number of token maps (in brackets).** MMD-CD and MMD-EMD scores are scaled by 10^3 and 10^2 .

Method	COV \uparrow		MMD \downarrow		1-NNA \downarrow	
	CD	EMD	CD	EMD	CD	EMD
Ours (2 scales)	62.98	63.62	3.569	7.944	83.12	82.31
Ours (4 scales)	65.98	65.32	3.081	7.613	82.94	81.34
Ours (8 scales)	66.31	65.73	3.027	7.583	82.36	81.07
Ours (11 scales)	66.80	65.93	2.900	7.543	82.10	80.92

Impact of Varying the Number of Token Maps Table 8 presents an analysis of how the number of token maps influences the performance of our 3D-WAG generation process. Specifically, we investigate the effect of varying the number of scales used to generate these token maps. The baseline 3D-WAG model, utilizing 11 token maps, achieves the highest Coverage (COV) scores, registering 66.80 for Chamfer Distance (CD) and 65.93 for Earth Mover’s Distance (EMD). Reducing the number of scales in the token maps results in a consistent, albeit slight, degradation in performance across all metrics. The COV scores for both CD and EMD decrease, indicating a minor reduction in the diversity of generated shapes. Similarly, the Minimum Matching Distance (MMD) scores increase from 2.900 to 3.569 for CD and from 7.543 to 7.944 for EMD, suggesting a subtle decline in the quality of the generation. A similar trend is observed in the 1-Nearest Neighbor Accuracy (1-NNA) scores, where fewer scales lead to diminished performance. These results highlight the inherent flexibility of the 3D-WAG approach. The number of token maps can be adjusted to strike a balance between generation quality and computational complexity. While the full configuration of 11 token maps yields the best overall performance, the variant using less token maps still produces compelling results. This makes it a viable option for deployments with limited computational resources. This adaptability underscores the versatility and practicality of our proposed framework.

Comparison with different quantization techniques In our experiments on the planes category of ShapeNet, Nearest Neighbor (NN) quantization [65] demonstrates superior performance across multiple evaluation metrics compared to other quantization-based approaches. As shown in Table 9, the NN quantization method achieves the highest Coverage (COV) scores of 66.80 and 65.93 for CD and EMD metrics, respectively, outperforming other quantization variants with LFQ [92] and FSQ [51]. Furthermore, NN quantization exhibits a favorable 1-NNA score and lower MMD scores (2.900 and 7.543 for CD and EMD), indicating better overall distribution matching between generated and real shapes.

14 Conditional Generation

Leveraging cross-attention mechanisms, we explore two applications of our 3DWAG autoregressive Transformer model: class-conditional generation and text-conditional generation, each utilizing annotated data during training to guide the generation process. In the class-

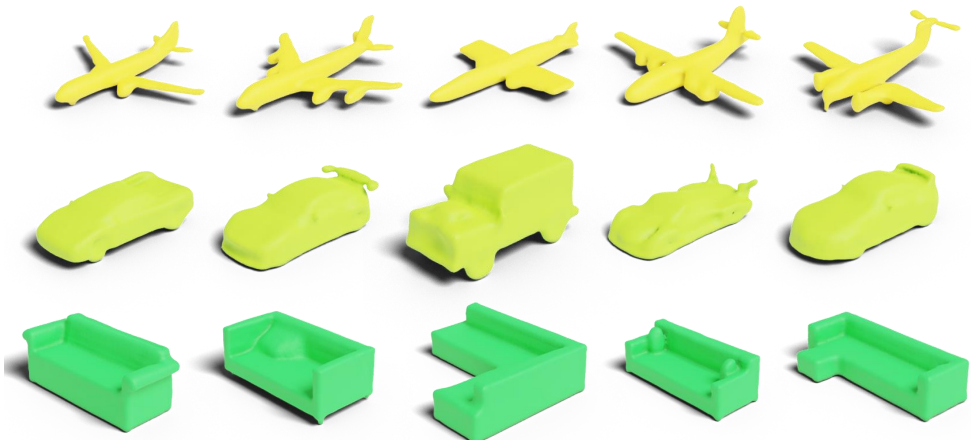


Figure 8: Examples of shape generation conditioned by class: airplane (top), car (middle), and sofa (bottom). Our model produces realistic and varied shapes within each category.

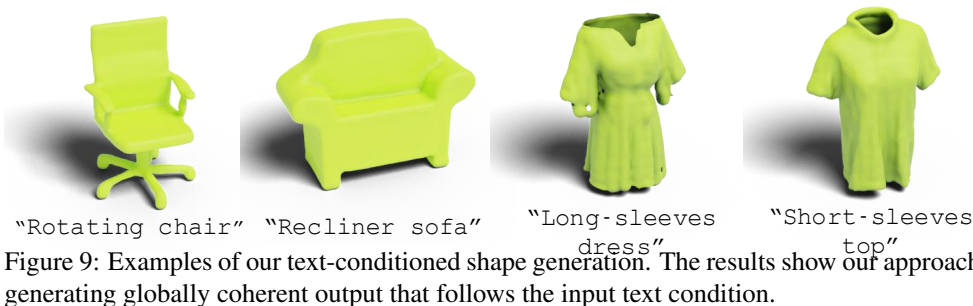


Figure 9: Examples of our text-conditioned shape generation. The results show our approach generating globally coherent output that follows the input text condition.

Table 9: **Shape generation on the planes dataset. Ablation over quantization techniques.** MMD-CD and MMD-EMD scores are scaled by 10^3 and 10^2 .

Method	COV \uparrow		MMD \downarrow		1-NNA \downarrow	
	CD	EMD	CD	EMD	CD	EMD
Ours + NN	66.80	65.93	2.900	7.543	82.01	80.92
Ours + LFQ	63.90	64.29	3.310	7.917	79.40	82.30
Ours + FSQ	65.50	64.87	3.109	7.840	79.20	79.88

conditional setting, we trained our model on 15 categories from the ShapeNet dataset, allowing it to generate shapes aligned with specific classes. Results for this class-conditional generation task are shown in Figure 8, showcasing the model’s ability to produce category-specific shapes with diverse details. We also finetuned the AR Transformer with text annotations using CLIP encoder to generate shapes using text prompts guidance on small ShapeNet and DeepFashion3D subsets. The resulting meshes can then be textured using the text input to produce realistic 3D assets. In this work, we employed Text2Tex model [14] to generate textures like also showcased in [102]. We showcase our results on the text-conditional generation task in Fig. 1 and 9. These results reveal the potential of our method in class and text-conditional generation.

References

- [1] Josh Achiam, Steven Adler, Sandhini Agarwal, Lama Ahmad, Ilge Akkaya, Florencia Leoni Aleman, Diogo Almeida, Janko Altenschmidt, Sam Altman, Shyamal Anadkat, et al. Gpt-4 technical report. *arXiv preprint arXiv:2303.08774*, 2023.
- [2] Rohan Anil, Andrew M Dai, Orhan Firat, Melvin Johnson, Dmitry Lepikhin, Alexandre Passos, Siamak Shakeri, Emanuel Taropa, Paige Bailey, Zhifeng Chen, et al. Palm 2 technical report. *arXiv preprint arXiv:2305.10403*, 2023.
- [3] Jinze Bai, Shuai Bai, Yunfei Chu, Zeyu Cui, Kai Dang, Xiaodong Deng, Yang Fan, Wenbin Ge, Yu Han, Fei Huang, et al. Qwen technical report. *arXiv preprint arXiv:2309.16609*, 2023.
- [4] Tom B Brown, Benjamin Mann, Nick Ryder, Melanie Subbiah, Jared D Kaplan, Prafulla Dhariwal, Arvind Neelakantan, Pranav Shyam, Girish Sastry, Amanda Askell, et al. Language models are few-shot learners. In *Advances in Neural Information Processing Systems*, volume 33, pages 1877–1901, 2020.
- [5] Ruojin Cai, Guandao Yang, Hadar Averbuch-Elor, Zekun Hao, Serge Belongie, Noah Snavely, and Bharath Hariharan. Learning gradient fields for shape generation. In *Computer Vision—ECCV 2020: 16th European Conference, Glasgow, UK, August 23–28, 2020, Proceedings, Part III 16*, pages 364–381. Springer, 2020.
- [6] Angel X Chang, Thomas Funkhouser, Leonidas Guibas, Pat Hanrahan, Qixing Huang, Zimo Li, Silvio Savarese, Manolis Savva, Shuran Song, Hao Su, et al. Shapenet: An information-rich 3D model repository. *arXiv preprint arXiv:1512.03012*, 2015.
- [7] Dave Zhenyu Chen, Yawar Siddiqui, Hsin-Ying Lee, Sergey Tulyakov, and Matthias Nießner. Text2tex: Text-driven texture synthesis via diffusion models. In *Proceedings of the IEEE/CVF International Conference on Computer Vision (ICCV)*, 2023.
- [8] Weikai Chen, Cheng Lin, Weiyang Li, and Bo Yang. 3psdf: Three-pole signed distance function for learning surfaces with arbitrary topologies. In *Proceedings of the IEEE/CVF Conference on Computer Vision and Pattern Recognition*, pages 18522–18531, 2022.
- [9] Yongwei Chen, Yushi Lan, Shangchen Zhou, Tengfei Wang, and Xingang Pan. Sar3d: Autoregressive 3d object generation and understanding via multi-scale 3d vqvae. In *CVPR*, 2025.
- [10] Zhiqin Chen and Hao Zhang. Learning implicit fields for generative shape modeling. In *Proceedings of the IEEE/CVF Conference on Computer Vision and Pattern Recognition*, pages 5939–5948, 2019.
- [11] An-Chieh Cheng, Xueting Li, Sifei Liu, Min Sun, and Ming-Hsuan Yang. Autoregressive 3d shape generation via canonical mapping. In *European Conference on Computer Vision (ECCV)*, 2022.
- [12] Yen-Chi Cheng, Hsin-Ying Lee, Sergey Tulyakov, Alexander G Schwing, and Liang-Yan Gui. Sdfusion: Multimodal 3d shape completion, reconstruction, and generation. In *Proceedings of the IEEE/CVF Conference on Computer Vision and Pattern Recognition*, pages 4456–4465, 2023.

- [13] Julian Chibane, Gerard Pons-Moll, et al. Neural unsigned distance fields for implicit function learning. *Advances in Neural Information Processing Systems*, 33:21638–21652, 2020.
- [14] Gene Chou, Yuval Bahat, and Felix Heide. Diffusion-sdf: Conditional generative modeling of signed distance functions. In *Proceedings of the IEEE/CVF International Conference on Computer Vision*, pages 2262–2272, 2023.
- [15] Aakanksha Chowdhery, Sharan Narang, Jacob Devlin, Maarten Bosma, Gaurav Mishra, Adam Roberts, Paul Barham, Hyung Won Chung, Charles Sutton, Sebastian Gehrmann, et al. Palm: Scaling language modeling with pathways. *Journal of Machine Learning Research*, 24(240):1–113, 2023.
- [16] Ingrid Daubechies. The wavelet transform, time-frequency localization and signal analysis. *IEEE transactions on information theory*, 36(5):961–1005, 1990.
- [17] Patrick Esser, Robin Rombach, and Bjorn Ommer. Taming transformers for high-resolution image synthesis. In *Proceedings of the IEEE/CVF Conference on Computer Vision and Pattern Recognition*, pages 12873–12883, 2021.
- [18] Ian Goodfellow, Jean Pouget-Abadie, Mehdi Mirza, Bing Xu, David Warde-Farley, Sherjil Ozair, Aaron Courville, and Yoshua Bengio. Generative adversarial networks. *Communications of the ACM*, 63(11):139–144, 2020.
- [19] Anchit Gupta, Wenhan Xiong, Yixin Nie, Ian Jones, and Barlas Oğuz. 3dgen: Triplane latent diffusion for textured mesh generation. *arXiv preprint arXiv:2303.05371*, 2023.
- [20] Amir Hertz, Or Perel, Raja Giryes, Olga Sorkine-Hornung, and Daniel Cohen-Or. Spaghetti: Editing implicit shapes through part aware generation. *ACM Transactions on Graphics (TOG)*, 41(4):1–20, 2022.
- [21] Jonathan Ho, Ajay Jain, and Pieter Abbeel. Denoising diffusion probabilistic models. *Advances in neural information processing systems*, 33:6840–6851, 2020.
- [22] Jordan Hoffmann, Sebastian Borgeaud, Arthur Mensch, Elena Buchatskaya, Trevor Cai, Eliza Rutherford, Diego de Las Casas, Lisa Anne Hendricks, Johannes Welbl, Aidan Clark, et al. Training compute-optimal large language models. *arXiv preprint arXiv:2203.15556*, 2022.
- [23] Fei Hou, Xuhui Chen, Wencheng Wang, Hong Qin, and Ying He. Robust zero level-set extraction from unsigned distance fields based on double covering. *ACM Transactions on Graphics*, 42(6), 2023.
- [24] Han Huang, Yulun Wu, Junsheng Zhou, Ge Gao, Ming Gu, and Yu-Shen Liu. Neusurf: On-surface priors for neural surface reconstruction from sparse input views. In *Proceedings of the AAAI Conference on Artificial Intelligence*, 2024.
- [25] Ka-Hei Hui, Ruihui Li, Jingyu Hu, and Chi-Wing Fu. Neural wavelet-domain diffusion for 3d shape generation. In *SIGGRAPH Asia 2022 Conference Papers*, pages 1–9, 2022.

- [26] Ka-Hei Hui, Aditya Sanghi, Arianna Rampini, Kamal Rahimi Malekshan, Zhengzhe Liu, Hooman Shayani, and Chi-Wing Fu. Make-a-shape: a ten-million-scale 3d shape model. In *Forty-first International Conference on Machine Learning*, 2024.
- [27] Le Hui, Rui Xu, Jin Xie, Jianjun Qian, and Jian Yang. Progressive point cloud deconvolution generation network. In *Computer Vision–ECCV 2020: 16th European Conference, Glasgow, UK, August 23–28, 2020, Proceedings, Part XV 16*, pages 397–413. Springer, 2020.
- [28] Chuan Jin, Tieru Wu, and Junsheng Zhou. Multi-grid representation with field regularization for self-supervised surface reconstruction from point clouds. *Computers & Graphics*, 2023.
- [29] Jared Kaplan, Sam McCandlish, Tom Henighan, Tom B Brown, Benjamin Chess, Rewon Child, Scott Gray, Alec Radford, Jeffrey Wu, and Dario Amodei. Scaling laws for neural language models. *arXiv preprint arXiv:2001.08361*, 2020.
- [30] Tero Karras, Miika Aittala, Timo Hellsten, Samuli Laine, Jaakko Lehtinen, and Frédo Durand. Elucidating the latent space of diffusion-based generative models. In *Advances in Neural Information Processing Systems*, volume 35, pages 25509–25521, 2022.
- [31] Diederik P Kingma and Max Welling. Auto-encoding variational bayes. *arXiv preprint arXiv:1312.6114*, 2013.
- [32] Durk P Kingma and Prafulla Dhariwal. Glow: Generative flow with invertible 1x1 convolutions. *Advances in neural information processing systems*, 31, 2018.
- [33] Marian Kleineberg, Matthias Fey, and Frank Weichert. Adversarial generation of continuous implicit shape representations. *arXiv preprint arXiv:2002.00349*, 2020.
- [34] Juil Koo, Seungwoo Yoo, Minh Hieu Nguyen, and Minhyuk Sung. Salad: Part-level latent diffusion for 3d shape generation and manipulation. In *Proceedings of the IEEE/CVF International Conference on Computer Vision*, pages 14441–14451, 2023.
- [35] Teven Le Scao, Angela Fan, Christopher Akiki, Ellie Pavlick, Suzana Ilić, Daniel Hesslow, Roman Castagné, Alexandra Sasha Luccioni, François Yvon, Matthias Gallé, et al. Bloom: A 176b-parameter open-access multilingual language model, 2023.
- [36] Doyup Lee, Chiheon Kim, Saehoon Kim, Minsu Cho, and Wook-Shin Han. Autoregressive image generation using residual quantization. In *Proceedings of the IEEE/CVF Conference on Computer Vision and Pattern Recognition*, pages 11523–11532, 2022.
- [37] Doyup Lee, Chiheon Kim, Saehoon Kim, Minsu Cho, and Wook-Shin Han. Autoregressive image generation using residual quantization. In *Proceedings of the IEEE/CVF Conference on Computer Vision and Pattern Recognition*, pages 11523–11532, 2022.
- [38] Muheng Li, Yueqi Duan, Jie Zhou, and Jiwen Lu. Diffusion-sdf: Text-to-shape via voxelized diffusion. In *Proceedings of the IEEE/CVF Conference on Computer Vision and Pattern Recognition*, pages 12642–12651, 2023.

- [39] Ruihui Li, Xianzhi Li, Ka-Hei Hui, and Chi-Wing Fu. Sp-gan: Sphere-guided 3d shape generation and manipulation. *ACM Transactions on Graphics (TOG)*, 40(4): 1–12, 2021.
- [40] Shujuan Li, Junsheng Zhou, Baorui Ma, Yu-Shen Liu, and Zhizhong Han. NeAF: Learning neural angle fields for point normal estimation. In *Proceedings of the AAAI Conference on Artificial Intelligence*, 2023.
- [41] Shujuan Li, Junsheng Zhou, Baorui Ma, Yu-Shen Liu, and Zhizhong Han. Learning continuous implicit field with local distance indicator for arbitrary-scale point cloud upsampling. In *Proceedings of the AAAI Conference on Artificial Intelligence*, 2024.
- [42] Xuanton Liu, Shaozhe Hao, Xianbiao Qi, Tianyang Hu, Jun Wang, Rong Xiao, and Yuan Yao. Elucidating the design space of language models for image generation. In *Proceedings of the 42nd International Conference on Machine Learning (ICML)*, 2025.
- [43] Yu-Tao Liu, Li Wang, Jie Yang, Weikai Chen, Xiaoxu Meng, Bo Yang, and Lin Gao. Neudf: Leaning neural unsigned distance fields with volume rendering. In *Proceedings of the IEEE/CVF Conference on Computer Vision and Pattern Recognition*, pages 237–247, 2023.
- [44] Xiaoxiao Long, Cheng Lin, Lingjie Liu, Yuan Liu, Peng Wang, Christian Theobalt, Taku Komura, and Wenping Wang. Neuraludf: Learning unsigned distance fields for multi-view reconstruction of surfaces with arbitrary topologies. In *Proceedings of the IEEE/CVF Conference on Computer Vision and Pattern Recognition (CVPR)*, pages 20834–20843, 2023.
- [45] William E Lorensen and Harvey E Cline. Marching cubes: A high resolution 3D surface construction algorithm. *ACM Siggraph Computer Graphics*, 21(4):163–169, 1987.
- [46] Shitong Luo and Wei Hu. Diffusion probabilistic models for 3d point cloud generation. In *Proceedings of the IEEE/CVF Conference on Computer Vision and Pattern Recognition*, pages 2837–2845, 2021.
- [47] Simian Luo, Xuelin Qian, Yanwei Fu, Yinda Zhang, Ying Tai, Zhenyu Zhang, Chengjie Wang, and Xiangyang Xue. Learning versatile 3d shape generation with improved ar models. *arXiv preprint arXiv:2303.14700*, 2023.
- [48] Baorui Ma, Haoge Deng, Junsheng Zhou, Yu-Shen Liu, Tiejun Huang, and Xinlong Wang. Geodream: Disentangling 2d and geometric priors for high-fidelity and consistent 3d generation. *arXiv preprint arXiv:2311.17971*, 2023.
- [49] Baorui Ma, Junsheng Zhou, Yu-Shen Liu, and Zhizhong Han. Towards better gradient consistency for neural signed distance functions via level set alignment. In *Proceedings of the IEEE/CVF Conference on Computer Vision and Pattern Recognition*, pages 17724–17734, 2023.
- [50] Tejaswini Medi, Jawad Tayyub, Muhammad Sarmad, Frank Lindseth, and Margret Keuper. Fullformer: Generating shapes inside shapes. In Ullrich Köthe and Carsten Rother, editors, *Pattern Recognition*, pages 147–162, Cham, 2024. Springer Nature Switzerland. ISBN 978-3-031-54605-1.

- [51] Fabian Mentzer, David Minnen, Eirikur Agustsson, and Michael Tschannen. Finite scalar quantization: Vq-vae made simple. In *International Conference on Learning Representations (ICLR) 2024*, 2024.
- [52] Lars Mescheder, Michael Oechsle, Michael Niemeyer, Sebastian Nowozin, and Andreas Geiger. Occupancy networks: Learning 3D reconstruction in function space. In *Proceedings of the IEEE/CVF Conference on Computer Vision and Pattern Recognition*, pages 4460–4470, 2019.
- [53] B Mildenhall, PP Srinivasan, M Tancik, JT Barron, R Ramamoorthi, and R Ng. NeRF: Representing scenes as neural radiance fields for view synthesis. In *European Conference on Computer Vision*, 2020.
- [54] Paritosh Mittal, Yen-Chi Cheng, Maneesh Singh, and Shubham Tulsiani. Autosdf: Shape priors for 3d completion, reconstruction and generation. In *Proceedings of the IEEE/CVF Conference on Computer Vision and Pattern Recognition*, pages 306–315, 2022.
- [55] Gimin Nam, Mariem Khelifi, Andrew Rodriguez, Alberto Tono, Linqi Zhou, and Paul Guerrero. 3d-ldm: Neural implicit 3d shape generation with latent diffusion models. *arXiv preprint arXiv:2212.00842*, 2022.
- [56] Charlie Nash, Yaroslav Ganin, SM Ali Eslami, and Peter Battaglia. Polygen: An autoregressive generative model of 3d meshes. In *International Conference on Machine Learning*, pages 7220–7229. PMLR, 2020.
- [57] Alex Nichol, Heewoo Jun, Prafulla Dhariwal, Pamela Mishkin, and Mark Chen. Point-e: A system for generating 3d point clouds from complex prompts. *arXiv preprint arXiv:2212.08751*, 2022.
- [58] Long Ouyang, Jeffrey Wu, Xu Jiang, Diogo Almeida, Carroll Wainwright, Pamela Mishkin, Chong Zhang, Sandhini Agarwal, Katarina Slama, Alex Ray, et al. Training language models to follow instructions with human feedback. *Advances in neural information processing systems*, 35:27730–27744, 2022.
- [59] Jeong Joon Park, Peter Florence, Julian Straub, Richard Newcombe, and Steven Lovegrove. DeepSDF: Learning continuous signed distance functions for shape representation. In *Proceedings of the IEEE/CVF Conference on Computer Vision and Pattern Recognition*, pages 165–174, 2019.
- [60] Alec Radford. Improving language understanding by generative pre-training, 2018.
- [61] Alec Radford, Jeffrey Wu, Rewon Child, David Luan, Dario Amodei, Ilya Sutskever, et al. Language models are unsupervised multitask learners. *OpenAI blog*, 1(8):9, 2019.
- [62] Amit Raj, Srinivas Kaza, Ben Poole, Michael Niemeyer, Nataniel Ruiz, Ben Mildenhall, Shiran Zada, Kfir Aberman, Michael Rubinstein, Jonathan T. Barron, Yuanzhen Li, and Varun Jampani. Dreambooth3d: Subject-driven text-to-3d generation. In *Proceedings of the IEEE/CVF International Conference on Computer Vision (ICCV)*, pages 2349–2359, October 2023. doi: 10.1109/ICCV51070.2023.00223.

- [63] Aditya Ramesh, Mikhail Pavlov, Gabriel Goh, Scott Gray, Chelsea Voss, Alec Radford, Mark Chen, and Ilya Sutskever. Zero-shot text-to-image generation. In *International conference on machine learning*, pages 8821–8831. Pmlr, 2021.
- [64] Ali Razavi, Aaron Van den Oord, and Oriol Vinyals. Generating diverse high-fidelity images with vq-vae-2. *Advances in neural information processing systems*, 32, 2019.
- [65] Ali Razavi, Aaron Van den Oord, and Oriol Vinyals. Generating diverse high-fidelity images with vq-vae-2. *Advances in neural information processing systems*, 32, 2019.
- [66] Pradyumna Reddy, Ismail Elezi, and Jiankang Deng. G3dr: Generative 3d reconstruction in imagenet. In *Proceedings of the IEEE/CVF Conference on Computer Vision and Pattern Recognition*, pages 9655–9665, 2024.
- [67] Xuanchi Ren, Jiahui Huang, Xiaohui Zeng, Ken Museth, Sanja Fidler, and Francis Williams. Xcube: Large-scale 3d generative modeling using sparse voxel hierarchies. In *Proceedings of the IEEE/CVF Conference on Computer Vision and Pattern Recognition*, pages 4209–4219, 2024.
- [68] Aditya Sanghi, Aliasghar Khani, Pradyumna Reddy, Arianna Rampini, Derek Cheung, Kamal Rahimi Malekshan, Kanika Madan, and Hooman Shayani. Wavelet latent diffusion (wala): Billion-parameter 3d generative model with compact wavelet encodings, 2024. URL <https://arxiv.org/abs/2411.08017>.
- [69] J Ryan Shue, Eric Ryan Chan, Ryan Po, Zachary Ankner, Jiajun Wu, and Gordon Wetzstein. 3d neural field generation using triplane diffusion. In *Proceedings of the IEEE/CVF Conference on Computer Vision and Pattern Recognition*, pages 20875–20886, 2023.
- [70] Edward J Smith and David Meger. Improved adversarial systems for 3d object generation and reconstruction. In *Conference on Robot Learning*, pages 87–96. PMLR, 2017.
- [71] Yang Song, Jascha Sohl-Dickstein, Diederik P Kingma, Abhishek Kumar, Stefano Ermon, and Ben Poole. Score-based generative modeling through stochastic differential equations. *arXiv preprint arXiv:2011.13456*, 2020.
- [72] Yongbin Sun, Yue Wang, Ziwei Liu, Joshua Siegel, and Sanjay Sarma. Pointgrow: Autoregressively learned point cloud generation with self-attention. In *Proceedings of the IEEE/CVF Winter Conference on Applications of Computer Vision*, pages 61–70, 2020.
- [73] Yu Sun, Shuohuan Wang, Shikun Feng, Siyu Ding, Chao Pang, Junyuan Shang, Jiaxiang Liu, Xuyi Chen, Yanbin Zhao, Yuxiang Lu, et al. Ernie 3.0: Large-scale knowledge enhanced pre-training for language understanding and generation. *arXiv preprint arXiv:2107.02137*, 2021.
- [74] Gemini Team, Rohan Anil, Sebastian Borgeaud, Jean-Baptiste Alayrac, Jiahui Yu, Radu Soricut, Johan Schalkwyk, Andrew M Dai, Anja Hauth, Katie Millican, et al. Gemini: a family of highly capable multimodal models. *arXiv preprint arXiv:2312.11805*, 2023.

- [75] Keyu Tian, Yi Jiang, Zehuan Yuan, Bingyue Peng, and Liwei Wang. Visual autoregressive modeling: Scalable image generation via next-scale prediction. In *Proceedings of the 38th Conference on Neural Information Processing Systems (NeurIPS 2024), Oral Poster Track*, 2024.
- [76] Hugo Touvron, Thibaut Lavril, Gautier Izacard, Xavier Martinet, Marie-Anne Lachaux, Timothée Lacroix, Baptiste Rozière, Naman Goyal, Eric Hambro, Faisal Azhar, et al. Llama: Open and efficient foundation language models. *arXiv preprint arXiv:2302.13971*, 2023.
- [77] Hugo Touvron, Louis Martin, Kevin Stone, Peter Albert, Amjad Almahairi, Yasmine Babaei, Nikolay Bashlykov, Soumya Batra, Prajjwal Bhargava, Shruti Bhosale, et al. Llama 2: Open foundation and fine-tuned chat models. *arXiv preprint arXiv:2307.09288*, 2023.
- [78] Aaron Van den Oord, Nal Kalchbrenner, Lasse Espeholt, Oriol Vinyals, Alex Graves, et al. Conditional image generation with pixelcnn decoders. *Advances in neural information processing systems*, 29, 2016.
- [79] Li Wang, Jie Yang, Weikai Chen, Xiaoxu Meng, Bo Yang, Jintao Li, and Lin Gao. Hsdf: Hybrid sign and distance field for modeling surfaces with arbitrary topologies. In *Advances in Neural Information Processing Systems*, 2022.
- [80] Si-Tong Wei, Rui-Huan Wang, Chuan-Zhi Zhou, Baoquan Chen, and Peng-Shuai Wang. Octgpt: Octree-based multiscale autoregressive models for 3d shape generation. In *Proceedings of the ACM SIGGRAPH 2025 Conference*, 2025.
- [81] Xin Wen, Junsheng Zhou, Yu-Shen Liu, Hua Su, Zhen Dong, and Zhizhong Han. 3D shape reconstruction from 2D images with disentangled attribute flow. In *Proceedings of the IEEE/CVF Conference on Computer Vision and Pattern Recognition*, pages 3803–3813, 2022.
- [82] Xin Wen, Peng Xiang, Zhizhong Han, Yan-Pei Cao, Pengfei Wan, Wen Zheng, and Yu-Shen Liu. PMP-Net++: Point cloud completion by transformer-enhanced multi-step point moving paths. *IEEE Transactions on Pattern Analysis and Machine Intelligence*, 45(1):852–867, 2023.
- [83] Jiajun Wu, Chengkai Zhang, Tianfan Xue, Bill Freeman, and Josh Tenenbaum. Learning a probabilistic latent space of object shapes via 3d generative-adversarial modeling. *Advances in neural information processing systems*, 29, 2016.
- [84] Shuang Wu, Youtian Lin, Yifei Zeng, Feihu Zhang, Jingxi Xu, Philip Torr, Xun Cao, and Yao Yao. Direct3d: Scalable image-to-3d generation via 3d latent diffusion transformer. In *NeurIPS 2024 Poster Session*, 2024.
- [85] Jianfeng Xiang, Zelong Lv, Sicheng Xu, Yu Deng, Ruicheng Wang, Bowen Zhang, Dong Chen, Xin Tong, and Jiaolong Yang. Structured 3d latents for scalable and versatile 3d generation. In *Proceedings of the IEEE/CVF Conference on Computer Vision and Pattern Recognition (CVPR)*, June 2025.

- [86] Peng Xiang, Xin Wen, Yu-Shen Liu, Yan-Pei Cao, Pengfei Wan, Wen Zheng, and Zhizhong Han. Snowflake point deconvolution for point cloud completion and generation with skip-transformer. *IEEE Transactions on Pattern Analysis and Machine Intelligence*, 45(5):6320–6338, 2023.
- [87] Bojun Xiong, Si-Tong Wei, Xin-Yang Zheng, Yan-Pei Cao, Zhouhui Lian, and Peng-Shuai Wang. Octfusion: Octree-based diffusion models for 3d shape generation. *Computer Graphics Forum (Eurographics Symposium on Geometry Processing)*, 2025. doi: 10.1111/cgf.70198.
- [88] Xingguang Yan, Liqiang Lin, Niloy J Mitra, Dani Lischinski, Daniel Cohen-Or, and Hui Huang. Shapeformer: Transformer-based shape completion via sparse representation. In *Proceedings of the IEEE/CVF Conference on Computer Vision and Pattern Recognition*, pages 6239–6249, 2022.
- [89] Guandao Yang, Xun Huang, Zekun Hao, Ming-Yu Liu, Serge Belongie, and Bharath Hariharan. Pointflow: 3d point cloud generation with continuous normalizing flows. In *Proceedings of the IEEE/CVF international conference on computer vision*, pages 4541–4550, 2019.
- [90] Jiahui Yu, Xin Li, Jing Yu Koh, Han Zhang, Ruoming Pang, James Qin, Alexander Ku, Yuanzhong Xu, Jason Baldridge, and Yonghui Wu. Vector-quantized image modeling with improved vqgan. *arXiv preprint arXiv:2110.04627*, 2021.
- [91] Jiahui Yu, Xin Li, Jing Yu Koh, Han Zhang, Ruoming Pang, James Qin, Alexander Ku, Yuanzhong Xu, Jason Baldridge, and Yonghui Wu. Vector-quantized image modeling with improved vqgan. In *International Conference on Learning Representations (ICLR) 2022*, 2022.
- [92] Lijun Yu, Jose Lezama, Nitesh Bharadwaj Gundavarapu, Luca Versari, Kihyuk Sohn, David Minnen, Yong Cheng, Agrim Gupta, Xiuye Gu, Alexander G Hauptmann, Boqing Gong, Ming-Hsuan Yang, Irfan Essa, David A Ross, and Lu Jiang. Language model beats diffusion - tokenizer is key to visual generation. In *The Twelfth International Conference on Learning Representations*, 2024. URL <https://openreview.net/forum?id=gzqrANCF4g>.
- [93] Qihang Yu, Ju He, Xueqing Deng, Xiaohui Shen, and Liang-Chieh Chen. Randomized autoregressive visual generation. *arXiv preprint arXiv:2411.00776*, 2024.
- [94] Biao Zhang, Jiapeng Tang, Matthias Nießner, and Peter Wonka. 3dshape2vecset: A 3d shape representation for neural fields and generative diffusion models. *ACM Trans. Graph.*, 42(4), jul 2023. ISSN 0730-0301. doi: 10.1145/3592442. URL <https://doi.org/10.1145/3592442>.
- [95] Lvmin Zhang, Anyi Rao, and Maneesh Agrawala. Adding conditional control to text-to-image diffusion models. In *Proceedings of the IEEE/CVF International Conference on Computer Vision (ICCV)*, pages 3813–3824. IEEE, 2023. doi: 10.1109/ICCV51070.2023.00355.
- [96] Wenyuan Zhang, Ruofan Xing, Yunfan Zeng, Yu-Shen Liu, Kanle Shi, and Zhizhong Han. Fast learning radiance fields by shooting much fewer rays. *IEEE Transactions on Image Processing*, 2023.

- [97] Xin-Yang Zheng, Hao Pan, Peng-Shuai Wang, Xin Tong, Yang Liu, and Heung-Yeung Shum. Locally attentional sdf diffusion for controllable 3d shape generation. *ACM Transactions on Graphics (SIGGRAPH)*, 42(4), 2023.
- [98] Junsheng Zhou, Baorui Ma, Yu-Shen Liu, Yi Fang, and Zhizhong Han. Learning consistency-aware unsigned distance functions progressively from raw point clouds. In *Advances in Neural Information Processing Systems (NeurIPS)*, 2022.
- [99] Junsheng Zhou, Xin Wen, Yu-Shen Liu, Yi Fang, and Zhizhong Han. Self-supervised point cloud representation learning with occlusion auto-encoder. *arXiv e-prints*, pages arXiv–2203, 2022.
- [100] Junsheng Zhou, Baorui Ma, Shujuan Li, Yu-Shen Liu, and Zhizhong Han. Learning a more continuous zero level set in unsigned distance fields through level set projection. In *Proceedings of the IEEE/CVF international conference on computer vision*, 2023.
- [101] Junsheng Zhou, Baorui Ma, Wenyuan Zhang, Yi Fang, Yu-Shen Liu, and Zhizhong Han. Differentiable registration of images and lidar point clouds with voxelpoint-to-pixel matching. In *Advances in Neural Information Processing Systems (NeurIPS)*, 2023.
- [102] Junsheng Zhou, Jinsheng Wang, Baorui Ma, Yu-Shen Liu, Tiejun Huang, and Xinlong Wang. Uni3d: Exploring unified 3d representation at scale. *International Conference on Learning Representations*, 2024.
- [103] Junsheng Zhou, Xin Wen, Baorui Ma, Yu-Shen Liu, Yue Gao, Yi Fang, and Zhizhong Han. 3d-oae: Occlusion auto-encoders for self-supervised learning on point clouds. *IEEE International Conference on Robotics and Automation (ICRA)*, 2024.
- [104] Junsheng Zhou, Weiqi Zhang, Baorui Ma, Kanle Shi, Yu-Shen Liu, and Zhizhong Han. Udiff: Generating conditional unsigned distance fields with optimal wavelet diffusion. In *Proceedings of the IEEE/CVF Conference on Computer Vision and Pattern Recognition*, pages 21496–21506, 2024.
- [105] Heming Zhu, Yu Cao, Hang Jin, Weikai Chen, Dong Du, Zhangye Wang, Shuguang Cui, and Xiaoguang Han. Deep fashion3d: A dataset and benchmark for 3d garment reconstruction from single images. In *Computer Vision–ECCV 2020: 16th European Conference, Glasgow, UK, August 23–28, 2020, Proceedings, Part I 16*, pages 512–530. Springer, 2020.